

A wet heterogeneous mantle creates a habitable world in the Hadean

Yoshinori Miyazaki^{1,2} & Jun Korenaga¹

¹*Department of Earth and Planetary Sciences, Yale University New Haven, CT 06511 USA*

²*Division of Geological and Planetary Sciences, California Institute of Technology, Pasadena, CA 91125 USA*

The Hadean eon, following the global-scale melting of the mantle^{1–3}, is expected to be a dynamic period, during which Earth experienced vastly different conditions. Geologic records, however, suggest that the surface environment of Earth was already similar to the present by the middle of the Hadean^{4,5}. Under what conditions a fiendish surface environment could turn into a habitable one remains uncertain⁶. Here we show that a hydrated mantle with small-scale chemical heterogeneity, created as a result of magma ocean solidification, is the key to ocean formation, the onset of plate tectonics, and the rapid removal of greenhouse gases, which are all essential to create a habitable environment on terrestrial planets. When the mantle is wet and dominated by high-magnesium pyroxenites, the removal of carbon dioxide from the atmosphere is expected to be >10 times faster than the case of a pyrolytic homogeneous mantle and could be completed within ~160 Myr. Such a chemically heterogeneous mantle would also produce oceanic crust rich in olivine, which is reactive with ocean water and promote serpentinization. Therefore, conditions similar to the Lost City Hydrothermal Field^{7–9} may have existed globally in the Hadean seafloor.

The Hadean Earth is often viewed as an uninhabitable world with a partially molten surface, active volcanism, and a hot steamy atmosphere. The picture of harsh surface conditions may be expected from the Moon-forming giant impact^{1,2} and the subsequent bombardment by leftover planetesimals¹⁰, but ancient geological records suggest that by \sim 4.3 Ga, the Earth's surface has become similar to the present-day environment with oceans and granitic crust^{4,5}. Hadean detrital zircons, enriched in heavy oxygen and yielding low melting temperatures, indicate that liquid water was already present at the Earth's surface. Furthermore, by the end of the Hadean, the global carbon cycle had likely stabilized the climate and maintained a surface temperature similar to the present day¹¹. The first 500 Myr of our planet, therefore, should have experienced a dramatic change in the climate, evolving quickly from being uninhabitable to habitable.

The troposphere during the early Hadean is believed to comprise greenhouse gases released during the solidification of a magma ocean¹²⁻¹⁶. The composition and redox state of the early atmosphere have been a subject of discussion^{17,18}, but Earth likely had a thick atmosphere of CO₂ and H₂O, which maintained an extreme climate on the early Earth^{13,19}. To create a habitable environment within the Hadean period, most of greenhouse gases must be removed from the atmosphere within the same timescale. Indeed, the atmospheric pressure of CO₂ is estimated to have been lower than 1 bar at the end of the Hadean^{11,20}. CO₂, the major constituent of greenhouse gases, can be sequestered into the Earth's interior by being transformed into carbonate minerals at ocean basins, and then subducted to the mantle⁶. It remains unclear, however, whether the sequestration was efficient enough to produce a habitable environment by \sim 4.0 Ga. In this study, this question is addressed by delineating the mode of geodynamics during the Hadean. We first investigate the

efficiency of mantle degassing during the solidification of a magma ocean, which is crucial for constraining the degree of hydration and thus the rheology of the Hadean mantle. We then turn to quantify the surface renewal rate and examine the rate of carbon sequestration.

Inefficient degassing of a magma ocean

First of all, an efficient degassing of the mantle is unlikely during the solidification of a magma ocean if a rheological transition in a partially molten medium is taken into account. A magma ocean behaves rheologically as solid when melt fraction becomes lower than a certain threshold (a typical value assumed in magma ocean studies is 40%^{19,21}), and if percolation is not rapid enough, volatiles would be trapped in the porous melt phase²². Volatiles, in particular water, would remain dissolved in the melt phase until melt fraction becomes lower than 0.2 wt%. Melt can contain water by more than 50 wt% at high pressures^{23,24} and that the initial water mantle inventory is estimated to be 0.04–0.1 wt%^{25,26}. Furthermore, the newly formed solid matrix would be continuously transported downwards by the Rayleigh-Taylor instability^{27,28}, and because the downwelling velocity of the instability is faster than melt percolation²¹, volatiles would be sequestered in the deep mantle. Therefore, water would either be trapped in the solid matrix as bubbles or would diffuse into the surrounding nominally anhydrous minerals. This indicates that a large fraction of water would remain in the mantle even after the solidification (Figure 1). If volatiles, behaving as incompatible elements, concentrates at the surface melt layer as magma ocean solidifies from the bottom to the top^{12–14}, volatile concentrations eventually exceed saturation levels, but such a high concentration of volatiles would not be reached if the rheological transition is taken into account.

The mass of atmosphere degassed from a magma ocean, therefore, is likely to be smaller than predicted in refs. ^{12–16}. With this effect of rheological transition on degassing²², we predict the evolution of atmospheric mass during magma ocean solidification using volatile partitioning between the atmosphere and the surface of a magma ocean. Because the solubilities of volatiles increase with pressure, those at the surface govern the volatile budget of the mantle. Figure 2a illustrates that while \sim 80% of the total carbon inventory would reside in the atmosphere, \sim 99% of water would remain in the mantle. Here we assume that the mantle contained between 0.04 and 0.1 wt% of H₂O (corresponding to \sim 1.2 and 3 ocean mass, respectively) and 200–500 ppm of CO₂, based on estimates for the present-day volatiles budget^{25,26}. We find that the atmospheric pressure of volatiles is mostly constant during the evolution because, when volatiles are trapped in the porous melt phase, the solidification process has a negligible effect on volatile concentration in the magma ocean. The atmospheric pressure increases by a small degree during the final stage of solidification as surface magma starts to solidify and volatiles become enriched in the melt phase (Figure 2a). Even so, with an initial water inventory is \sim 1.2 ocean, the surface water is limited to \sim 0.011 ocean mass with a partial pressure of \sim 7 bar (Figure 2a). On the other hand, a large fraction of CO₂ would be degassed to the atmosphere from the beginning of the evolution because CO₂ is more insoluble than H₂O in silicate melt^{22,29}. Our partitioning model predicts that the partial pressure of CO₂ would be \sim 110 and 290 bar with initial concentrations of 200 and 500 ppm, respectively.

Surface water is likely supplemented by another degassing after the disappearance of the melt-dominated layer. When the surface of a magma ocean behaves rheologically as melt (Fig-

ure 1a), high convective heat flux, supported by low melt viscosity, maintains a high surface temperature above 1000 °C (Figure 2b)^{13,15}. When cooling proceeds and the surface becomes rheologically solid (Figure 1b), however, convective heat flux decreases by orders of magnitude, and a 1-D atmospheric model suggests the surface temperature drops discontinuously to a temperature below the mantle solidus. At this point, the Rayleigh-Taylor instability, which can happen rapidly and frequently²⁸, should have cooled the mantle, changing the mantle thermal structure to be adiabatic from superadiabatic, and solid-state convection would govern the cooling thereafter^{21,30}. Timescale comparison suggests that solid-state convection is slower than upward melt percolation in the upper mantle (see Methods), so residual melt in the shallow upper mantle would percolate upward and erupt to the surface. Based on a mantle melting model, we predict that the top \sim 4 GPa of the upper mantle (Figure 1b, Extended Data Figure 1a) was partially molten at the beginning of solid-state convection, and volatiles in this layer was likely extracted to the atmosphere. For the case of \sim 0.04 wt% initial water content, a total of \sim 0.06 ocean mass of water is released to the atmosphere, creating \sim 36 atm of water vapor atmosphere (Figures 2a, Table S1). This exceeds a threshold of \sim 0.05 ocean mass to form water oceans when the atmosphere contains \sim 200 bar of CO₂¹⁹, so the presence of ocean is thus plausible immediately after the solidification of a magma ocean. The surface temperature exceeds \sim 100 °C due to greenhouse effect, yet liquid water is stabilized by high atmospheric pressure. At the same time, the mantle would still contain a large fraction of water and is expected to be hydrated, lowering the viscosity^{31,32} of the Hadean mantle.

Rapid plate motion of a hydrated and chemically heterogeneous mantle

We now turn to the second question of carbon sequestration. With the presence of oceans, the operation of plate tectonics is theoretically possible even in the early Hadean^{33,34}, so CO₂ could be removed by the formation and subduction of carbonate minerals. The partial pressure of CO₂ is estimated to have been below 1 bar by the end of the Hadean^{11,20}, so >100 bar of CO₂ has to be transported back into the mantle. The frequent renewal of the surface by rapid cooling has been proposed as a possible mechanism^{6,35}, but contrary to a common belief, a hotter mantle in the past points to more sluggish plate motion because of thicker depleted lithospheric mantle^{33,36}. Slow plate motion of a hotter mantle, in fact, is corroborated with a range of geological records³⁷⁻³⁹. Moreover, the Hadean mantle could have been chemically stratified as a result of an overturn after the solidification of magma ocean, with iron-rich dense materials at the bottom¹². If so, the mantle would be resistant to thermal convection⁴⁰, and plate motion would be even slower, if not totally absent. A hotter mantle in the Hadean, therefore, does not necessarily indicate the rapid sequestration of CO₂.

We propose that rapid recycling is possible with a chemically heterogeneous mantle, which results from the fractional crystallization of a magma ocean²⁸. The differentiation of a magma ocean is driven by the settling and sedimentation of a liquidus mineral, bridgemanite, at the base of the melt-dominated layer. Consequently, high-Mg# (defined as molar Mg/(Mg+Fe)×100) and SiO₂-rich materials would constitute the lower mantle, whereas the upper mantle would be comprised of residual iron-rich dense materials (Figure 3a). Our scaling analysis suggests that such

a gravitationally unstable structure is subject to small-scale Rayleigh-Taylor instabilities with a length scale shorter than 100 km²⁸. At the end of solidification, iron-rich materials would thus have existed as small blobs embedded in a high-Mg# pyroxenite matrix (Figure 3a). As explained in detail later, such a mantle with small-scale heterogeneity would not develop thick depleted lithospheric mantle, so rapid plate motion and efficient carbon sequestration could be achieved. In the following, we estimate the surface evolution timescales for both homogeneous and heterogeneous mantles. Our results suggest that the chemically heterogeneous mantle is more compatible with creating a habitable environment by the end of the Hadean.

The chemically heterogeneous mantle is predicted to experience limited dehydration at mid-ocean ridges. Modeling of magma ocean solidification suggests that the pyroxenite matrix has an average Mg# of 94 and constitutes ~75% of the mantle²⁸. The high-Mg# pyroxenite yields a higher solidus than a homogeneous pyrolytic mantle, and with a mantle potential temperature of 1600 °C, the Rhyolite-MELTS and pMELTS models^{41,42} predict that the initial depth of melting is ~4 GPa with 0.1 wt% of water (Extended Data Figure 1a). As the mantle undergoes fractional melting, the pyroxenite matrix becomes mostly dehydrated at ~2 GPa and forms a depleted lithospheric mantle of 40 km thickness (Extended Data Figure 1b). Iron-rich blobs would also melt during their upwelling, but because they are of small scale, their melting would not contribute to producing a uniformly thick depleted lithospheric mantle. Stress necessary to bend plates is smaller with thinner depleted lithospheric mantle, whereas stress due to the negative buoyancy of plates increases under a higher potential temperature, so the operation of plate tectonics is plausible (see Methods). Pyrolite, on the other hand, starts to melt at a depth deeper than 10 GPa, and

because it is rich in olivine, which is less compatible with water than pyroxene, a pyrolytic mantle would dehydrate faster than pyroxenite. Crust and depleted lithospheric mantle are thus estimated to be as thick as \sim 26 km and \sim 145 km, respectively, at a mantle temperature 250 K hotter than the present (Figure 3b, Extended Data Figure 2).

Thin depleted lithospheric mantle is a key for rapid plate motion under a hotter mantle. Because the depleted lithospheric mantle is drier and thus stiffer, thicker lithosphere results in slower convection than the present-day mantle⁴³ (Figure 3c). Also, the presence of thick buoyant crust would require a longer cooling time for plate to be negatively buoyant⁴⁴, which would further limit the plate velocity. The scaling of plate tectonic convection⁴⁵ suggests that, for a pyrolytic mantle, average plate velocity would remain the same as the present at a potential temperature of 1600 °C. In contrast, the depleted lithospheric mantle of chemically heterogeneous mantle is thin enough to allow for rapid plate motion, and its crust is only marginally chemically buoyant because of crust produced from iron-rich blobs, which has a density greater than 3500 kg m⁻³ (Extended Data Table 1) and would help to negate the chemical buoyancy of oceanic crust. Plate velocity for the heterogeneous mantle is estimated to be \sim 50 cm yr⁻¹ (Figure 3c), and ocean basins would be renewed every \sim 9 Myr, allowing the rapid recycling of carbonate minerals. It is noted that, if the mantle had degassed completely during magma ocean solidification, the whole mantle would be dry and stiff, and its viscosity would be \sim 50 times higher than that of the present-day mantle, even considering the effect of a higher temperature^{31,32}. Plate velocity would be limited to \sim 2 cm yr⁻¹ (see Methods), and the surface renewal rate becomes smaller than that of a pyrolytic mantle.

Furthermore, the Hadean seafloor could store a greater amount of carbonate minerals because seawater circulating through oceanic crust has a higher CO₂ content. The solubility of CO₂ is higher by at least an order of magnitude under >100 bar than the present-day atmosphere⁴⁶, and thus the alteration of upper oceanic crust was likely significant. When Ca and Mg in the top 500 m of the crust, a layer with high porosity, were used to form carbonates, an equivalent of ~22 bar could be stored to the mantle, which is 9 times larger than the present day value of ~2.5 bar⁴⁷. The *P-T* path of the Hadean slab would resemble the present-day young subduction zones (Extended Data Figure 3), so some fraction of carbonates may melt and return to the surface. Yet, even assuming that half of subducted carbonates are recycled, 200 bar of CO₂ could be removed from the atmosphere within ~160 Myr (Figure 4). In contrast, if the mantle were pyrolytic, sluggish plate motion would limit the sequestration of CO₂. Our model predicts that the atmospheric CO₂ remains higher than 10 bar with a surface temperature over 100 °C for ~1.5 Gyr (Figure 4), which fails to explain the evolution of Earth's atmosphere and surface conditions. If the mantle was pyrolytic in the Hadean, the removal of CO₂ from the atmosphere is unlikely to be completed by the end of Archean.

A high iron-rich olivine content in crust of the chemically heterogeneous mantle (Extended Data Table 1) would promote serpentinization reaction⁴⁸, which has an important implication for the earliest life on Earth⁴⁹. Serpentinization releases hydrogen and methane by reducing water (Figure 4a), and the anaerobic oxidation of methane is considered to have supported nascent life forms before the beginning of photosynthesis. Methane released by seafloor serpentinization is also observed now at the Lost City hydrothermal vent field (LCHF)⁷ located along the Mid-Atlantic

Ridge. Microorganisms that use H_2 and CH_4 as chemical energy are known to create diverse biological communities in the LCHF^{8,9}, and thus it has been considered as an analog environment to a place where life first appeared on our planet. Given that rocks constituting the LCHF are rich in olivine and have low Si content, a wide exposure of pyroxenite may have created a similar environment to the LCHF at most of the seafloor in the early Hadean. Alkaline conditions may also develop in an environment resembling hydrothermal vents, and combined with the high dissolution rate of olivine, abiotic synthesis of ribose may have occurred⁵⁰.

The aftermath of magma ocean solidification has a profound impact on characterizing the surface environment during the Hadean. Given that a habitable environment has emerged by ~ 4.0 Gyr ago, the Hadean evolution is explained more naturally by the mantle with a chemically heterogeneous structure. Small-scale heterogeneities would eventually be homogenized with high-Mg# pyroxenite as convective mixing proceeds, but homogenization likely takes a few tens to hundreds million years to complete⁵¹. In the meantime, rapid plate motion would have continued. A faster plate motion accompanies a larger flux of upwelling mantle at mid-ocean ridges, so volatiles (including greenhouse gases) in the mantle would efficiently be released to the atmosphere. As sequestration removes CO_2 from the atmosphere, the intake and release of CO_2 would balance after some time, setting an initial condition for the Archean evolution. Also, residual CO_2 may have reacted with hydrogen produced by serpentinization to create a reduced atmosphere (Figure 4). This may explain the potentially high abundance of CH_4 in the Archean atmosphere²⁰. On the other hand, hydrous minerals are vulnerable to dehydration upon subduction, so a rapid plate motion would result in a net increase in surface water through degassing at ridges. Given a higher

processing rate than the present-day mantle, the Hadean mantle would have dried out in \sim 500 Myr (see Methods), and an initially small ocean mass would have increased to the present-day level or higher by the beginning of the Archean. These are order-of-magnitude arguments but are consistent with the prominent features of the Archean Earth^{20,26,33}. Our study provides a new perspective on the evolution of Hadean surface environment by bringing together the models of magma ocean solidification, atmospheric evolution, and mantle convection.

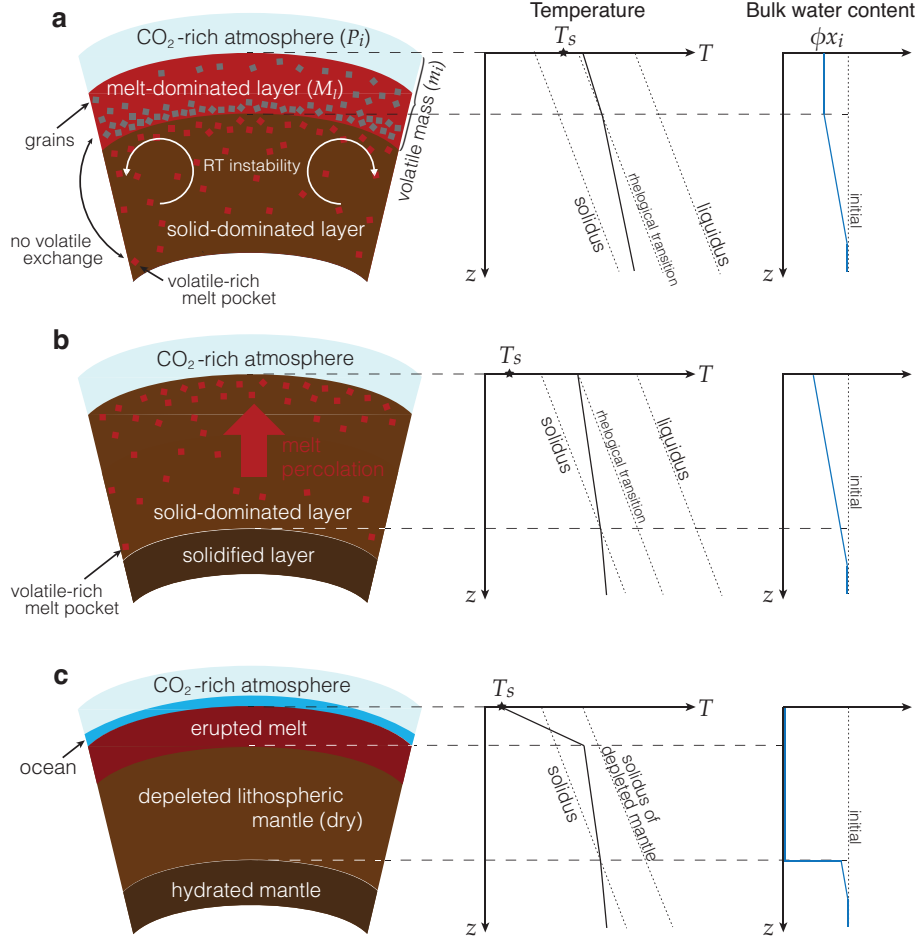


Figure 1: Schematic illustration of how a magma ocean solidifies with the evolution of atmosphere. Only the shallow mantle is illustrated here. **a.** A magma ocean solidifies from the bottom, and the porous melt phase emerges in regions where melt fraction falls below a critical value. Volatiles in the deep mantle are stored in such a residual melt phase instead of being concentrated near the surface. Note that a magma ocean has two rheologically distinct layers, the melt- and solid-dominated. The former is mixed by rapid convection, whereas the latter by the Rayleigh-Taylor instability, both creating an adiabatic thermal profile. Parameters used in Equation (1) (Methods) are labeled to corresponding reservoirs. **b.** When the melt-dominated layer diminishes, convective heat flux plummets, and the surface temperature (star) drops below the mantle solidus. Melt percolation governs the subsequent evolution because solid-state convection is slow. **c.** Erupted melt from the residual melt phase forms a solidified lid, leaving a depleted dry mantle behind. By releasing dissolved volatiles to the atmosphere, the atmosphere contains an enough amount of volatile to form oceans on a cooled surface. The deeper region of the mantle is completely solidified and thus would not degas by percolation. Although it is not shown here, the deeper region contains small-scale iron-rich blobs because we consider a chemically heterogeneous mantle in this study (Figure 3a).

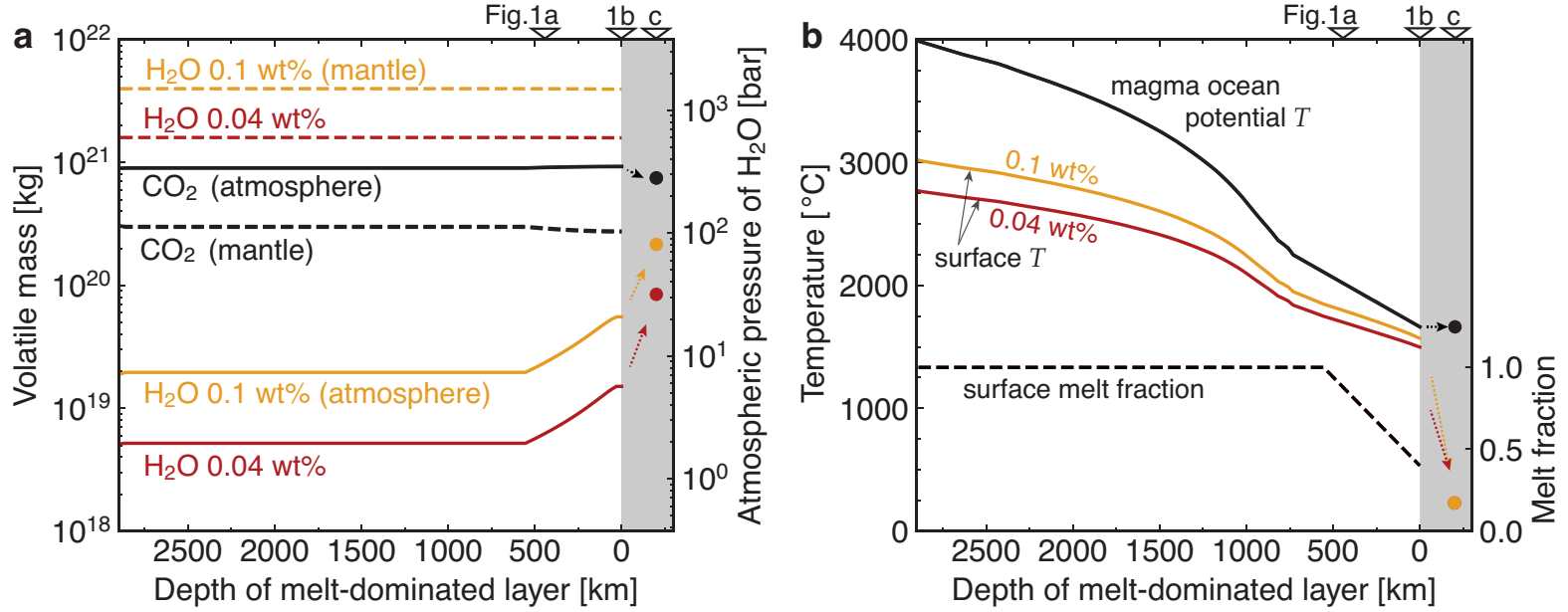


Figure 2: Mantle degassing considering the effect of the rheological transition. Figures are shown as a function of the depth of a melt-dominated layer, and the system evolves from left to right as solidification proceeds. **a.** The volatile budgets of H_2O (colored) and CO_2 (black) in the atmosphere (solid) and the mantle (dashed). **b.** Surface temperature (colored), the potential temperature of magma ocean (black), and the surface melt fraction (dashed). The corresponding atmospheric pressures of H_2O are shown in the right axis. The H_2O contents are coded by color as 0.04 (red) and 0.1 (yellow), corresponding to 1.2 and 3 ocean mass, respectively. Here, the initial CO_2 concentration in the mantle is set to 300 ppm. Dots in shaded regions indicate the state after the complete solidification as described in Figure 1c. For concentrations in the mantle, values after the complete solidification are not shown because only the uppermost layer is affected by melt percolation, and volatiles concentrations in the deeper region remain unchanged.

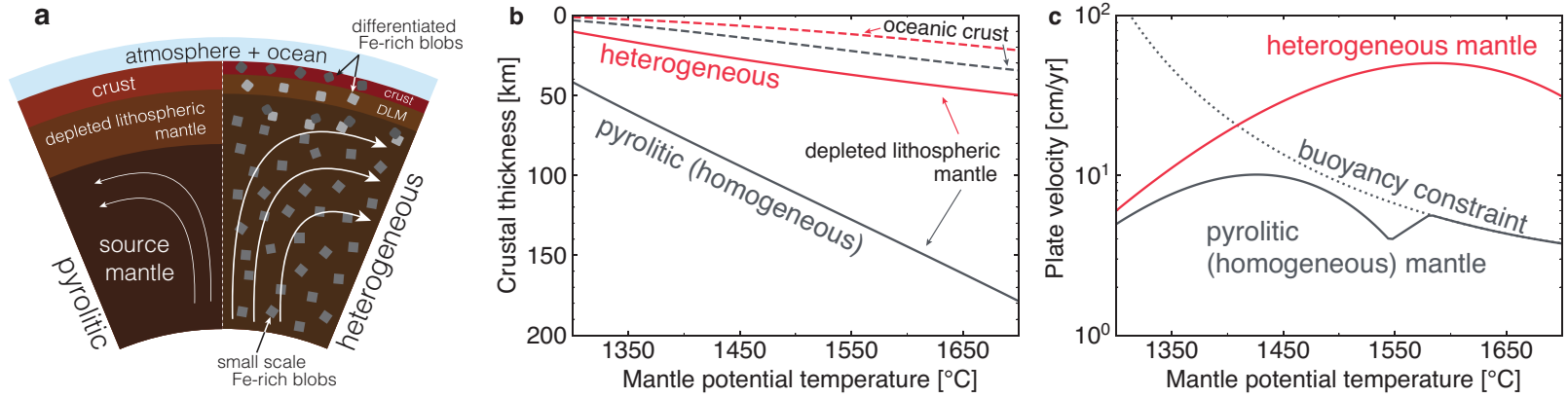


Figure 3: Crustal thickness and plate velocity of chemically heterogeneous and pyrolytic (homogeneous) mantles. **a.** Schematic illustration of the near-surface structure for pyrolytic (left) and chemically heterogeneous (right) mantles. **b.** Estimated thicknesses of oceanic crust (dashed) and depleted lithospheric mantle (solid lines) for different mantle potential temperatures. Color indicates chemically heterogeneous (red) and pyrolytic homogeneous mantles (gray). **c.** Plate velocities for different mantle potential temperatures. A stiff depleted lithospheric mantle is thicker for a pyrolytic homogeneous mantle, resulting in more sluggish plate motion for a hotter mantle. The plate velocity of a mantle hotter than 1590 °C would be further limited by a buoyancy constraint (dotted). With thicker oceanic crust, a longer cooling time or a thicker thermal boundary layer is required for plate to be negatively buoyant. A mantle water content of 0.1 wt% is assumed here.

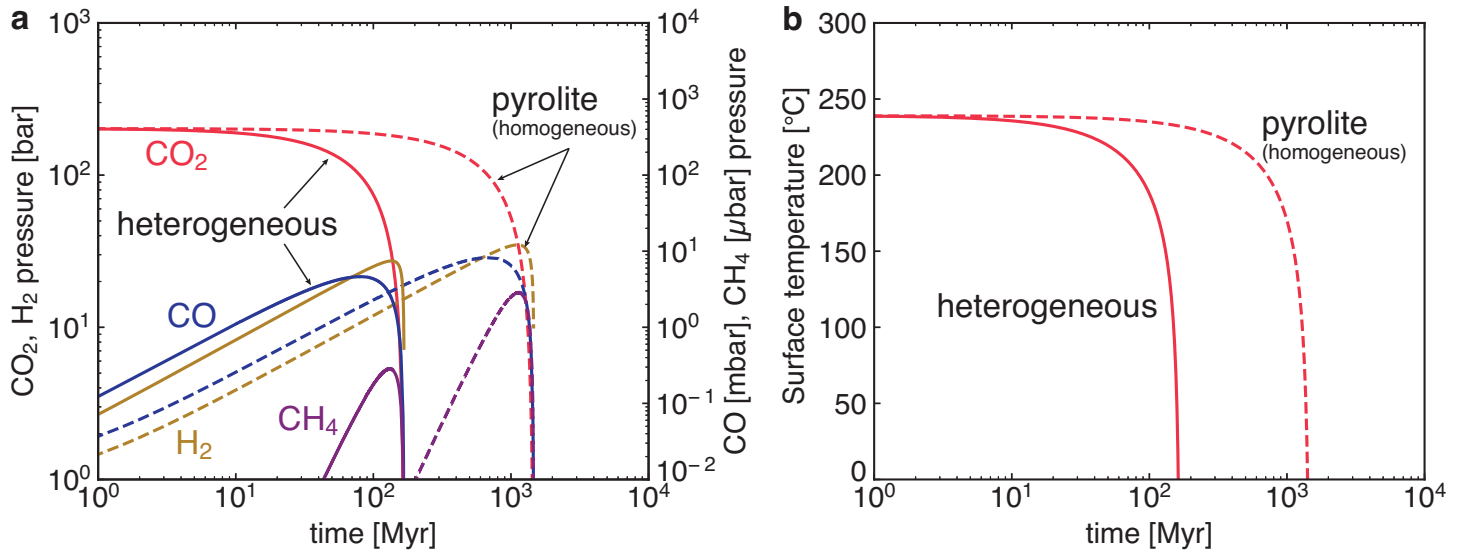


Figure 4: **Evolutions of atmospheric composition and surface temperature after the onset of plate tectonics.**

a. Atmospheric evolution is shown for the cases of chemically heterogeneous (solid) and homogeneous (pyrolitic) mantles (dashed). Color indicates gaseous species: CO_2 (red), CO (blue), H_2 (yellow), and CH_4 (purple). The initial amount of CO_2 is set to 200 bar, which is the amount degassed from a magma ocean with 300 ppm of CO_2 , and the model calculations are performed until all CO_2 are sequestered to the mantle. b. Surface temperature evolution based on an 1-D atmospheric model.

1. Matsui, T. & Abe, Y. Evolution of an impact-induced atmosphere and magma ocean on the accreting Earth. *Nature* **319**, 303–305 (1986).
2. Tonks, W. B. & Melosh, H. J. Magma ocean formation due to giant impacts. *Journal of Geophysical Research* **98**, 5319–5333 (1993).
3. Canup, R. M. & Asphaug, E. Origin of the Moon in a giant impact near the end of the Earth's formation. *Nature* **412**, 708–712 (2001).
4. Wilde, S. A., Valley, J. W., Peck, W. H. & Graham, C. M. Evidence from detrital zircons for the existence of continental crust and oceans on the Earth 4.4 Gyr ago. *Nature* **409**, 175–178 (2001).
5. Harrison, T. M. The Hadean crust: Evidence from >4 Ga zircons. *Annual Review of Earth and Planetary Sciences* **37**, 479–505 (2009).
6. Sleep, N. H. & Zahnle, K. Carbon dioxide cycling and implications for climate on ancient Earth. *Journal of Geophysical Research* **106**, 1373–1399 (2001).
7. Kelley, D. S. *et al.* A serpentinite-hosted ecosystem: The Lost City Hydrothermal Field. *Science* **307**, 1428–1434 (2005).
8. Proskurowski, G. *et al.* Abiogenic hydrocarbon production at Lost City Hydrothermal Field. *Science* **319**, 604–607 (2008).

9. Klein, F., Grozeva, N. G. & Seewald, J. S. Abiotic methane synthesis and serpentinization in olivine-hosted fluid inclusions. *Proceedings of the National Academy of Sciences* **116**, 17666–17672 (2019).
10. Raymond, S. N., Schlichting, H. E., Hersant, F. & Selsis, F. Dynamical and collisional constraints on a stochastic late veneer on the terrestrial planets. *Icarus* **226**, 671–681 (2013).
11. Krissansen-Totton, J., Arney, G. N. & Catling, D. C. Constraining the climate and ocean pH of the early Earth with a geological carbon cycle model. *Proceedings of the National Academy of Sciences* **115**, 4105–4110 (2018).
12. Elkins-Tanton, L. T. Linked magma ocean solidification and atmospheric growth for Earth and Mars. *Earth and Planetary Science Letters* **271**, 181–191 (2008).
13. Lebrun, T. *et al.* Thermal evolution of an early magma ocean in interaction with the atmosphere. *Journal of Geophysical Research: Planets* **118**, 1155–1176 (2013).
14. Hamano, K., Abe, Y. & Genda, H. Emergence of two types of terrestrial planet on solidification of magma ocean. *Nature* **497**, 607–610 (2013).
15. Salvador, A. *et al.* The relative influence of H₂O and CO₂ on the primitive surface conditions and evolution of rocky planets. *Journal of Geophysical Research: Planets* **122**, 1458–1486 (2017).
16. Bower, D. J. *et al.* Linking the evolution of terrestrial interiors and an early outgassed atmosphere to astrophysical observations. *Astronomy and Astrophysics* **631**, A103 (2019).
1904.08300.

17. Hirschmann, M. M. Magma ocean influence on early atmosphere mass and composition. *Earth and Planetary Science Letters* **341-344**, 48–57 (2012).
18. Deng, J., Du, Z., Karki, B. B., Ghosh, D. B. & Lee, K. K. A magma ocean origin to divergent redox evolutions of rocky planetary bodies and early atmospheres. *Nature Communications* **11**, 2007 (2020).
19. Abe, Y. Physical state of the very early Earth. *Lithos* **30**, 223–235 (1993).
20. Catling, D. C. & Zahnle, K. J. The Archean atmosphere. *Science Advances* **6**, eaax1420 (2020).
21. Solomatov, V. S. Magma oceans and primordial mantle differentiation. In *Treatise on Geophysics*, vol. 9, 91–119 (Elsevier B.V., 2007).
22. Hier-Majumder, S. & Hirschmann, M. M. The origin of volatiles in the Earth’s mantle. *Geochemistry, Geophysics, Geosystems* **18**, 3078–3092 (2017).
23. Kawamoto, T. & Holloway, J. R. Melting temperature and partial melt chemistry to H₂O-saturated mantle peridotite to 11 gigapascals. *Science* **276**, 240–243 (1997).
24. Katz, R. F., Spiegelman, M. & Langmuir, C. H. A new parameterization of hydrous mantle melting. *Geochemistry, Geophysics, Geosystems* **4**, 1073 (2003).
25. Hirschmann, M. M. & Dasgupta, R. The H/C ratios of Earth’s near-surface and deep reservoirs, and consequences for deep Earth volatile cycles. *Chemical Geology* **262**, 4–16 (2009).

26. Korenaga, J., Planavsky, N. J. & Evans, D. A. D. Global water cycle and the coevolution of the Earth's interior and surface environment. *Philosophical Transactions of the Royal Society A* **375**, 20150393 (2017).

27. Maurice, M. *et al.* Onset of solid-state mantle convection and mixing during magma ocean solidification. *Journal of Geophysical Research: Planets* **122**, 577–598 (2017).

28. Miyazaki, Y. & Korenaga, J. On the timescale of magma ocean solidification and its chemical consequences: 2. Compositional differentiation under crystal accumulation and matrix compaction. *Journal of Geophysical Research: Solid Earth* **124**, 3399–3419 (2019).

29. Blank, J. G. & Brooker, R. A. Experimental studies of carbon dioxide in silicate melts: solubility, speciation, and stable carbon isotope behavior. In Carroll, M. R. & Holloway, J. R. (eds.) *Reviews in Mineralogy and Geochemistry*, 157–186 (Mineralogical Society of America, 1994).

30. Abe, Y. Thermal evolution and chemical differentiation of the terrestrial magma ocean. *Geophysical Monograph* **74** **14**, 41–54 (1993).

31. Hirth, G. & Kohlstedt, D. L. Water in the oceanic upper mantle: Implications for rheology, melt extraction and the evolution of the lithosphere. *Earth and Planetary Science Letters* **144**, 93–108 (1996).

32. Jain, C., Korenaga, J. & Karato, S.-i. Global analysis of experimental data on the rheology of olivine aggregates. *Journal of Geophysical Research: Solid Earth* **124**, 310–334 (2019).

33. Korenaga, J. Thermal evolution with a hydrating mantle and the initiation of plate tectonics in the early Earth. *Journal of Geophysical Research* **116**, B12403 (2011).
34. Korenaga, J. Plate tectonics and surface environment: Role of the oceanic upper mantle. *Earth-Science Reviews* **205**, 103185 (2020).
35. Zahnle, K. *et al.* Emergence of a habitable planet. *Space Science Reviews* **129**, 35–78 (2007).
36. Korenaga, J. Energetics of mantle convection and the fate of fossil heat. *Geophysical Research Letters* **30**, 1437 (2003).
37. Bradley, D. C. Passive margins through earth history. *Earth-Science Reviews* **91**, 1–26 (2008).
38. Herzberg, C., Condie, K. & Korenaga, J. Thermal history of the Earth and its petrological expression. *Earth and Planetary Science Letters* **292**, 79–88 (2010).
39. Pehrsson, S. J., Eglington, B. M., Evans, D. A., Huston, D. & Reddy, S. M. Metallogeny and its link to orogenic style during the Nuna supercontinent cycle. *Geological Society Special Publication* **424**, 83–94 (2016).
40. Plesa, A.-C., Tosi, N. & Breuer, D. Can a fractionally crystallized magma ocean explain the thermo-chemical evolution of Mars? *Earth and Planetary Science Letters* **403**, 225–235 (2014).
41. Ghiorso, M. S., Hirschmann, M. M., Reiners, P. W. & Kress, V. C. The pMELTS: A revision of MELTS for improved calculation of phase relations and major element partitioning related to partial melting of the mantle to 3 GPa. *Geochemistry, Geophysics, Geosystems* **3** (2002).

42. Gualda, G. A., Ghiorso, M. S., Lemons, R. V. & Carley, T. L. Rhyolite-MELTS: A modified calibration of MELTS optimized for silica-rich, fluid-bearing magmatic systems. *Journal of Petrology* **53**, 875–890 (2012).

43. Korenaga, J. Archean geodynamics and the thermal evolution of Earth. In Benn, K., Mareschal, J.-C. & Condie, K. (eds.) *Archean Geodynamics and Environments*, 7–32 (AGU, Washington, D.C., 2006).

44. Davies, G. F. On the emergence of plate tectonics. *Geology* **20**, 963–966 (1992).

45. Korenaga, J. Scaling of plate tectonic convection with pseudoplastic rheology. *Journal of Geophysical Research* **115**, B11405 (2010).

46. Diamond, L. W. & Akinfiev, N. N. Solubility of CO₂ in water from -1.5 to 100°C and from 0.1 to 100 MPa: Evaluation of literature data and thermodynamic modelling. *Fluid Phase Equilibria* **208**, 265–290 (2003).

47. Alt, J. C. & Teagle, D. A. The uptake of carbon during alteration of ocean crust. *Geochimica et Cosmochimica Acta* **63**, 1527–1535 (1999).

48. Sleep, N. H., Meibom, A., Fridriksson, T., Coleman, R. G. & Bird, D. K. H₂-rich fluids from serpentinization: Geochemical and biotic implications. *Proceedings of the National Academy of Sciences* **101**, 12818–12823 (2004).

49. Schulte, M., Blake, D., Hoehler, T. & McCollom, T. Serpentinization and its implications for life on the early Earth and Mars. *Astrobiology* **6**, 364–376 (2006).

50. Lambert, J. B., Gurusamy-Thangavelu, S. A. & Ma, K. The silicate-mediated formose reaction: Bottom-up synthesis of sugar silicates. *Science* **327**, 984–986 (2010).
51. Davies, G. F. Gravitational depletion of the early Earth’s upper mantle and the viability of early plate tectonics. *Earth and Planetary Science Letters* **243**, 376–382 (2006).

52. Nakajima, S., Hayashi, Y.-Y. & Abe, Y. A study on the “runaway greenhouse effect” with a one-dimensional radiative-convective equilibrium model. *Journal of the Atmospheric Sciences* **49**, 2256–2266 (1992).

53. Zahnle, K. J., Kasting, J. F. & Pollack, J. B. Evolution of a steam atmosphere during Earth’s accretion. *Icarus* **74**, 62–97 (1988).

54. Dullien, F. A. L. *Porous media: Fluid transport and pore structure* (Academic Press, San Diego, 1992), 2 edn.

55. Zahnle, K. J., Lupu, R., Dobrovolskis, A. & Sleep, N. H. The tethered Moon. *Earth and Planetary Science Letters* **427**, 74–82 (2015).

56. Tronnes, R. G. & Frost, D. J. Peridotite melting and mineral-melt partitioning of major and minor elements at 22–24.5 GPa. *Earth and Planetary Science Letters* **197**, 117–131 (2002).

57. Corgne, A., Liebske, C., Wood, B. J., Rubie, D. C. & Frost, D. J. Silicate perovskite-melt partitioning of trace elements and geochemical signature of a deep perovskitic reservoir. *Geochimica et Cosmochimica Acta* **69**, 485–496 (2005).

58. Parsons, B. Causes and consequences of the relation between area and age of the ocean floor. *Journal of Geophysical Research* **87**, 289–302 (1982).

59. Zhang, G., Mei, S. & Song, M. Effect of water on the dislocation creep of enstatite aggregates at 300 MPa. *Geophysical Research Letters* **47**, e2019GL085895 (2020).

60. Aubaud, C., Hauri, E. H. & Hirschmann, M. M. Hydrogen partition coefficients between nominally anhydrous minerals and basaltic melts. *Geophysical Research Letters* **31**, L20611 (2004).

61. de Capitani, C. & Petrakakis, K. The computation of equilibrium assemblage diagrams with Theriak/Domino software. *American Mineralogist* **95**, 1006–1016 (2010).

62. Christensen, U. R. Thermal evolution models for the Earth. *Journal of Geophysical Research* **90**, 2995–3007 (1985).

63. Korenaga, J. Thermal cracking and the deep hydration of oceanic lithosphere : A key to the generation of plate tectonics? *Journal of Geophysical Research* **112**, B05408 (2007).

64. Tackley, P. J. Mantle geochemical geodynamics. In *Treatise on Geophysics, Second Edition*, vol. 7, 521–585 (Elsevier B.V., 2015).

65. Dasgupta, R. & Hirschmann, M. M. The deep carbon cycle and melting in Earth’s interior. *Earth and Planetary Science Letters* **298**, 1–13 (2010).

66. Kelemen, P. B. & Manning, C. E. Reevaluating carbon fluxes in subduction zones, what goes down, mostly comes up. *Proceedings of the National Academy of Sciences* **112**, E3997–E4006 (2015).

67. Sleep, N. H., Zahnle, K. & Neuhoff, P. S. Initiation of clement surface conditions on the earliest Earth. *Proceedings of the National Academy of Sciences* **98**, 3666–3672 (2001).

68. Peterson, M. N. A. Calcite: Rates of dissolution in a vertical profile in the central Pacific. *Science* **154**, 1542–1544 (1966).

69. Andersson, A. J. The oceanic CaCO_3 cycle. In Holland, H. D. & Turekian, K. (eds.) *Treatise on Geochemistry, Second Edition*, vol. 8, 519–542 (Elsevier, 2014).

70. Kelemen, P. B. *et al.* Rates and mechanisms of mineral carbonation in peridotite: Natural processes and recipes for enhanced, in situ CO_2 capture and storage. *Annual Review of Earth and Planetary Sciences* **39**, 545–576 (2011).

71. Syracuse, E. M., van Keken, P. E. & Abers, G. A. The global range of subduction zone thermal models. *Physics of the Earth and Planetary Interiors* **183**, 73–90 (2010).

72. Dasgupta, R., Hirschmann, M. M. & Withers, A. C. Deep global cycling of carbon constrained by the solidus of anhydrous, carbonated eclogite under upper mantle conditions. *Earth and Planetary Science Letters* **227**, 73–85 (2004).

73. Korenaga, J. On the extent of mantle hydration caused by plate bending. *Earth and Planetary Science Letters* **457**, 1–9 (2017).

74. Miller, N. C., Lizarralde, D., Collins, J. A., Holbrook, W. S. & Van Avendonk, H. J. Limited mantle hydration by bending faults at the middle America trench. *Journal of Geophysical Research: Solid Earth* **126** (2021).

75. Miyazaki, Y. & Korenaga, J. Effects of chemistry on vertical dust motion in early protoplanetary disks. *The Astrophysical Journal* **849**, 41 (2017).

76. Wirth, E. A. & Korenaga, J. Small-scale convection in the subduction zone mantle wedge. *Earth and Planetary Science Letters* **357-358**, 111–118 (2012).

77. Johnson, S. S., Mischna, M. A., Grove, T. L. & Zuber, M. T. Sulfur-induced greenhouse warming on early Mars. *Journal of Geophysical Research: Planets* **113**, E08005 (2008).

78. Lyubetskaya, T. & Korenaga, J. Chemical composition of Earth's primitive mantle and its variance: 1. Method and results. *Journal of Geophysical Research* **112**, B03211 (2007).

79. Gale, A., Dalton, C. A., Langmuir, C. H., Su, Y. & Schilling, J.-G. The mean composition of ocean ridge basalts. *Geochemistry, Geophysics, Geosystems* **14**, 489–518 (2013).

Methods

1 Degassing of magma ocean

Volatile partitioning between magma ocean and atmosphere We solve for the degassing of the mantle based on volatile partitioning between the atmosphere and the mantle. The atmosphere and the melt phase at the surface of a magma ocean are assumed to be in equilibrium, so for each volatile component, the concentration in the surface magma, x_i , is calculated from the solubility at its partial pressure, P_i . When the mass of the melt-dominated layer is M_l , the following mass balance holds¹⁶

$$x_i \phi M_l + \frac{\mu_i}{\bar{\mu}} \frac{4\pi R_e^2}{g} P_i = m_i, \quad (1)$$

where ϕ is melt fraction at the surface of a magma ocean, μ_i is the molar mass of either H₂O or CO₂, $\bar{\mu}$ is the mean molar mass of the atmosphere, R_e is the Earth's radius, g is gravity, and m_i is the total mass of the volatile under consideration in the melt-dominated layer and the atmosphere (see Figure 1a). The first term indicates the volatile budget in the melt-dominated layer, where $x_s \phi$ is the bulk volatile concentration in a crystal-melt mixture of the melt-dominated layer. As a result of rapid convection, this bulk volatile concentration is assumed to be constant throughout the melt-dominated layer. For solubility, we adopt the parameterization of Blank and Brooker²⁹, and

$$P_{\text{H}_2\text{O}}(x_{\text{H}_2\text{O}}) = \left(\frac{x_{\text{H}_2\text{O}}}{6.8 \times 10^{-8}} \right)^{1.42} \quad (2)$$

and

$$P_{\text{CO}_2}(x_{\text{CO}_2}) = \left(\frac{x_{\text{CO}_2}}{4.4 \times 10^{-12}} \right) \quad (3)$$

are used for water and CO₂, respectively. Note that $x_{\text{H}_2\text{O}}$ and x_{CO_2} are given in terms of mass fraction. Melt fraction at the surface ϕ is calculated from the surface temperature, which is estimated using a 1-D atmospheric model of ref. ⁵² (see Supplementary for details). The surface temperature, T_s , is a function of the atmospheric mass and composition and the net outgoing infrared radiation, and the outgoing radiation, F_{out} , is described as the sum of absorbed sunlight and convective heat flux^{21,53}:

$$F_{\text{out}} = (1 - A)F_{\odot} + 0.089 \frac{k_T(T_m - T_s)}{d} Ra^{1/3}, \quad (4)$$

where A is the albedo, F_{\odot} is solar flux (values discussed later in Atmospheric Model), k is thermal conductivity (4 W m⁻¹ K⁻¹), T_m is mantle potential temperature, d is the depth of the melt-dominated layer, and Ra is the Rayleigh number of the melt-dominated layer. This value is set as F_{\uparrow} at $\tau = 0$ in the atmospheric model.

At the beginning of the evolution, the entire mantle is assumed to be melt-dominated, and M_l is set to the mass of the entire mantle. The initial mass of volatile m_i is calculated from the initial volatiles concentration, which is assumed to be 0.04–0.1 wt% for water and 200–500 ppm for CO₂. As a magma ocean solidifies and the melt-dominated layer shrinks, the solid-dominated layer grows from the bottom of the mantle. Volatiles would be trapped in the porous melt phase of the solid-dominated layer, so when ΔM of the mantle solidifies to be solid-dominated and the melt-dominated layer shrinks by Δd , $\Delta M_l x_s \phi$ of volatiles would be removed from the volatile budget of the melt-dominated layer m_i :

$$m_i(d - \Delta d) = m_i(d) - \Delta M_l x_s \phi. \quad (5)$$

Equations (1–5) are solved as the melt-dominated layer solidifies until $d = 0$. The evolution of

volatile budget is summarized in Table S1 in Supplementary.

Degassing of a magma ocean during the last phase of its solidification When the melt-dominated layer disappears, the upper part of the mantle, while being rheologically solid, remains partially molten. When upward melt percolation is faster than solid-state convection, volatiles contained in the partially molten layer are expected to be released to the atmosphere (Figure 1b). As partial melt approaches the surface and solidifies, volatiles concentrate in the residual melt phase. Volatiles eventually exceed the saturation limit, and thus volatiles in the near-surface region would have degassed efficiently. We compare the timescales of melt percolation, t_{perc} , and convection, t_{conv} , to determine the depth where melt and volatiles can be extracted to the surface.

The timescale of melt percolation from a depth of D to the surface is given by

$$t_{\text{perc}} = \frac{D}{v_{\text{perc}}}, \quad (6)$$

where v_{perc} is percolation velocity⁵⁴,

$$v_{\text{perc}} = \frac{d^2 g \Delta \rho}{150 \eta_l} \frac{\phi^2}{1 - \phi}. \quad (7)$$

Here d denotes the grain size of solid matrix, g is gravity, $\Delta \rho$ is density difference between the melt and solid phases, η_l is melt viscosity, and ϕ is melt fraction. For $d = 1 \text{ mm}^2$, $g = 9.8 \text{ m s}^{-2}$, $\Delta \rho = 400 \text{ kg m}^{-3}$, and $\eta_l = 1 \text{ Pa s}$,

$$t_{\text{perc}} \sim 2.5 \left(\frac{D}{200 \text{ km}} \right) \left(\frac{0.01}{\phi} \right)^2 \text{ Myr.} \quad (8)$$

The convective timescale is scaled using plate velocity as

$$t_{\text{conv}} = \frac{D}{v_s} \sim 4.0 \left(\frac{D}{200 \text{ km}} \right) \left(\frac{v_s}{5.0 \text{ cm yr}^{-1}} \right) \text{ Myr,} \quad (9)$$

where v_s is plate velocity, whose formulation is described in the later section. These suggest that a partially molten layer with $\phi > 0.01$ likely becomes depleted in porous melt and thus volatiles.

The thickness and structure of the partially molten layer are estimated from an adiabat with a melt fraction of 0.4 at the surface because the rapid Rayleigh-Taylor instability^{27,28} likely maintained an adiabatic temperature profile within the solid-dominated layer. A melt fraction of 0.4 marks the rheological transition of a partially molten medium^{21,30}. We utilize the Rhyolite-MELTS model⁴² and a mantle melting model of ref. ²⁴ to derive the adiabatic temperature gradient (see Supplementary for details). The depth of partially molten layer varies with water content, but for a pyrolytic mantle with 0.1 wt% water, the melt-dominated layer disappears at a potential temperature of ~ 1600 °C, and melt fraction becomes lower than 0.01 at a depth of ~ 5 GPa assuming fractional melting (Extended Data Figure 2; the implementation of fractional melting is described later) .

The chemically heterogeneous mantle consists of a mixture of iron-rich blobs and a high-Mg# pyroxenite matrix, and thus its average melt fraction should be 0.4 when the mantle starts to behave rheologically as solid. The magma ocean model of ref. ²⁸ suggests that the mass fraction of iron-rich blobs is about a quarter of the entire mantle. Considering that iron-rich blobs have a higher degree of melting, the melt-dominate layer disappeared when the potential temperature reached ~ 1625 °C, and the region with melt fraction higher than 0.01 extended up to a depth of ~ 4 GPa (Extended Data Figure 1). For simplicity, we assume that the entire mantle became rheologically solid at a potential temperature of 1600 °C for both chemically homogeneous and heterogeneous mantles, and these thermal structures are adopted as initial conditions for subse-

quent calculations.

It is noted that a small amount of degassing by episodic eruptions may also take place during the transition from magma ocean to solid-state convection. Our model assumes that the Rayleigh-Taylor instability efficiently cools the solid-dominated layer^{27,28}, and the layer maintains an adiabatic thermal profile within the timescale of magma ocean solidification. Cooling, however, could be inhibited by tidal heating⁵⁵, and such heat may be released by episodic eruptions in addition to convective heat flux after the solidification of the mantle surface. Consequently, water degassing could be promoted, and ocean mass may increase rapidly. Yet, the interplay between tidal heating, cooling by the Rayleigh-Taylor instability, and melt percolation remains unconstrained, and future work is required to quantify the degree of degassing during this period. Episodic eruptions, however, would not affect the overall mode of mantle dynamics. Erupted melt would be recycled to the mantle by plate tectonics, and the rate of carbon sequestration is expected to remain unchanged from our model results.

The composition of the chemically heterogeneous mantle The fractional crystallization of a magma ocean produces a structure dominated by the high-Mg# matrix with small iron-rich blobs (Figure 3a, Extended Data Figure 1d). Ref. ²⁸ estimated that the ternary composition of the high-Mg# matrix is on average MgO 41.7 wt%, FeO 4.4 wt%, and SiO₂ 53.9 wt%, whereas that of iron-rich blobs is MgO 41.0 wt%, FeO 20.6 wt%, and SiO₂ 38.3 wt%. The Mg# of the two components are \sim 94 and \sim 77, respectively, resulting in a difference in density and melting temperature. It is noted that iron-rich blobs make up \sim 25% of the heterogeneous mantle, and the

average composition of the mantle is consistent with the pyrolytic mantle.

The solidus of such a high-Mg# matrix is expected to be higher than that of a pyrolytic mantle, and we estimate the solidus temperature using the Rhyolite-MELTS model⁴². To predict the mineralogy of high-Mg# matrix, the Al₂O₃ and CaO contents are estimated using a partitioning model described in the following paragraph. Combining the results of the partitioning model with the ternary composition, we obtain an estimate of MgO 39.5 wt%, FeO 4.1 wt%, SiO₂ 51.3 wt%, Al₂O₃ 3.5 wt%, and CaO 1.5 wt% for the high-Mg# matrix, which results in a mineral assemblage of 70 wt% pyroxene, 25 wt% olivine, 5 wt% spinel at 1500 °C and 1.2 GPa. For Fe-rich blobs, a composition of MgO 37.8 wt%, FeO 19.0 wt%, SiO₂ 35.3 wt%, Al₂O₃ 3.7 wt%, and CaO 4.1 wt% is predicted, resulting in a mineral assemblage of 84 wt% olivine, 8 wt% of merwinite, 6 wt% of spinel, and 2 wt% of periclase. The melt fraction of the two components are shown in Extended Data Figure 1.

To predict the concentrations of Al₂O₃ and CaO, we construct an element partitioning model within the magma ocean, assuming that all newly crystals in the melt-dominated layer would stack at the base of the layer to form a rheologically rigid layer (Figure 1a). This is the same as crystal accumulation in the model of ref. ²⁸. In a terrestrial magma ocean, crystals forming below the liquidus are predominantly bridgmanite under lower-mantle pressures, so at each time step, we calculate the amount of newly-formed bridgmanite and estimate the partitioning of Al₂O₃ and CaO between melt and bridgmanite. Bridgmanite would be incorporated in the growing rheologically rigid layer, which includes some amount of melt because the compaction of crystal-melt mixture can take place only slowly. The partitioning coefficients between melt and bridgmanite are esti-

mated from the experimental results of refs. ⁵⁶ and ⁵⁷, and we adopt values of $D_{\text{Al/Si}} = 0.78$ and $D_{\text{Ca/Si}} = 0.16$.

The mantle is initially assumed to be entirely molten, and we run the model while newly formed bridgmanite is heavier than the remaining melt. The model of ref. ²⁸ suggests that, when the depth of melt-dominated layer reaches 500 km, bridgmanite becomes lighter than the remaining melt and compositional fractionation ceases. The partitioning model indicates that the lower mantle, which eventually evolves into the high-Mg# matrix, would be depleted in CaO but shows little change in the Al_2O_3 content from the initial after the solidification (Extended Data Figure 4). We thus estimate that the high-Mg# matrix would have concentrations of $\text{Al}_2\text{O}_3 3.6 \pm 0.7$ wt% and CaO 1.51 ± 0.11 wt%.

2 Atmospheric evolution after the formation of oceans

In our model, the removal of CO_2 from the atmosphere is governed by the formation of carbonates at ocean basins, which are sequestered to the mantle by subduction. At each time step, we remove CO_2 by carbonation formation, release H_2 by serpentinization, and update the surface temperature based on the new atmospheric pressure and composition (see paragraph Atmospheric model). This procedure is repeated until all CO_2 in the atmosphere are sequestered to the mantle.

The timescale of CO_2 removal is assumed to be the same with that of ocean basins renewal, so the removal rate is proportional to the surface renewal rate and is inversely proportional to plate velocity. With the current plate construction rate⁵⁸ of $3.4 \text{ km}^2 \text{ yr}^{-1}$, which corresponds to the average plate velocity of 5 cm yr^{-1} , the entire ocean basin is renewed every 90 Myr. The amount

of carbonate formed at the seafloor is estimated based on the assumption that Ca and Mg silicates in the top 500 m of oceanic crust reacted with CO_2^{35} , and we estimate that the Hadean seafloor contained ~ 14 bar of CO_2 , whereas current basaltic crust holds ~ 2.5 bar of atmospheric CO_2 . Details are discussed in the later section.

Plate velocity When plate tectonics is operating, plate velocity, v_s , can be estimated from mantle heat flux, Q , as

$$v_s = v_{s,0} \left(\frac{Q}{Q_0} \frac{\Delta T_0}{\Delta T} \right)^2, \quad (10)$$

where ΔT is the temperature difference between the surface and mantle. The subscript 0 indicates the present-day values; $v_{s,0}$ is 5 cm yr^{-1} , Q_0 is 38 TW, and ΔT_0 is 1350 K. Mantle heat flux Q is calculated based on the scaling of ref. ⁴⁵, which includes the effect of dehydration stiffening of depleted lithospheric mantle. Convective heat flux Q is given by

$$Q = Nu \frac{k_T A \Delta T}{L} \quad (11)$$

where Nu is the Nusselt number, A is the surface area of Earth, and L is the mantle depth. The Nusselt number Nu is calculated as⁴⁵

$$Nu = 2 \left(\frac{Ra_i}{Ra_c} \right)^{1/3} \Delta \eta_L^{-1/3}, \quad (12)$$

where Ra_i is the internal Rayleigh Number, Ra_c is the critical Rayleigh number ($\equiv 1000$), and $\Delta \eta_L$ is the lithospheric viscosity contrast. The internal Rayleigh number is defined as

$$Ra_i = \frac{\alpha \rho g \Delta T L^3}{\kappa \eta}, \quad (13)$$

where α is thermal expansivity, ρ is mantle density, and κ is thermal diffusivity. Mantle viscosity, η , changes with temperature with an activation energy, E , of 300 kJ/mol, and the reference viscosity is set to 10^{19} Pa s at 1350 °C. The lithospheric viscosity contrast $\Delta\eta_L$ changes with the thickness of depleted lithospheric mantle, h_m , as

$$\Delta\eta_L = \Delta\eta_{L,\text{ref}} \exp \left[\ln(\Delta\eta) \min \left(1, \frac{h_m}{6h_{\text{ref}}} \right) \right], \quad (14)$$

where $\Delta\eta_{L,\text{ref}}$ is the reference viscosity contrast, $\Delta\eta$ is the viscosity contrast induced by mantle dehydration, and h_{ref} is the thickness of thermal boundary layer in the absence of dehydration stiffening, L/Nu_{ref} . The reference viscosity contrast $\Delta\eta_{L,\text{ref}}$ is parameterized as⁴⁵

$$\Delta\eta_{L,\text{ref}} = \exp \left(0.326 \left(\frac{\mu}{\alpha\Delta T} \right)^{0.647} \theta \right), \quad (15)$$

where μ is an effective friction coefficient and θ is a nondimensionalized activation energy (known as the Frank-Kamenetskii parameter),

$$\theta = \frac{E\Delta T}{RT_p^2}, \quad (16)$$

where R is the universal gas constant and T_p is mantle potential temperature. To reproduce the present-day heat flux of 38 TW, we adopt $\Delta\eta = 100$ and $\mu = 0.025$. These values indicate that a dry mantle has a viscosity higher by 100 times than the present-day convecting mantle, and a mantle with a potential temperature of 1600 °C is 20 times less viscous than that of 1350 °C with the same degree of dehydration. It is noted that the rheology of the chemically heterogeneous mantle is expected to be similar to that of a pyrolytic mantle. The pyroxenite matrix contains 25% of olivine, which is a threshold for a phase to be interconnected, and thus its rheology would also be governed by olivine. Even if olivine grains are not interconnected, enstatite aggregates probably

have similar viscosity to olivine aggregates under dislocation creep at temperatures expected for the Hadean mantle⁵⁹.

The difference in plate velocity between the chemically homogeneous and heterogeneous mantles arises from h_m . Because a hotter mantle with the same composition would melt by a larger degree, the value of h_m for a pyrolytic mantle would be thicker than the present. To predict the thickness of dehydrated lithosphere, a fractional melting model is constructed based on the melting model of ref. ²⁴. Assuming that a fraction of the partial melt escapes to the surface with each increment of new melting (see the caption of Extended Figures 1 and 2), the depleted lithospheric mantle would thicken to \sim 140 km (4.5 GPa) for a mantle potential temperature of 1600 °C, from \sim 60 km (2 GPa), which is the thickness for the present-day depleted lithospheric mantle (Extended Data Figure 2). On the other hand, the value of h_m for the chemically heterogeneous mantle is predicted to be \sim 40 km based on the Rhyolite-MELTS model⁴², and the initial depth of melting has been checked with the pMELTS model⁴¹. Because the high-Mg# pyroxenite starts to melt at a shallower depth than a pyrolytic homogeneous mantle, and also because the partition coefficient of water between pyroxene and melt is larger than that between olivine and melt, we estimate that the mantle would not be completely dehydrated until 2 GPa. A value of 0.02 is adopted for water partitioning between the pyroxenite and melt, and 0.005 for partitioning between pyrolyte and melt⁶⁰. It is noted that iron-rich blobs would melt at a depth deeper than 10 GPa (Extended Data Figure 1c), but the melting of blobs only creates locally depleted regions and thus is unlikely to affect the overall value of h_m .

A buoyancy constraint would further limit the plate velocity for a pyrolytic mantle^{43,44} (Fig-

ure 3c). The thicknesses of buoyant basaltic crust and depleted lithospheric mantle increase as the mantle becomes hotter, and thus the thermal boundary layer needs to grow sufficiently thick for plate to be negatively buoyant. The densities of oceanic crust and depleted lithospheric mantle are estimated using a model of ref. ⁴³, and to become negatively buoyant, the subduction age of plate is set to the critical age of lithosphere. Such a buoyancy constraint, however, does not apply for the case of chemically heterogeneous mantle. The melting of high-Mg# pyroxenite matrix would also produce buoyant oceanic crust at the surface, but its thickness is \sim 4 km, 15% of crust formed under a pyrolytic (Figure 3b). Also, crust created by the melting of iron-rich blobs would act as a weight within a crust to promote subduction because iron-rich crust would have an Mg# of 56 and a density over 3500 kg m^{-3} (Extended Data Table 1). Fe-rich blobs start to melt at a deeper depth, so its crust would have an average thickness of \sim 11 km. The crust of the chemically heterogeneous mantle would not be uniform, but the average crustal thickness is predicted to be \sim 15 km, \sim 70% of which originates from Fe-rich blobs. It is noted that the density of partial melt from iron-rich blobs is estimated to be 3000 kg m^{-3} , which is still lower than the high-Mg# matrix. Partial melt from iron-rich blobs would thus migrate upwards within the high-Mg# matrix. The density difference between iron-rich melt and the matrix is approximately four times smaller than that between partial melt from the matrix and the matrix itself, so these two kinds of partial melt may migrate upward without much mixing. The large fraction of the iron-rich crust may be situated below the high-Mg# crust, but some amount of iron-rich crust would be exposed at the surface, promoting H_2 and CH_4 production at the seafloor. Crustal composition is calculated by averaging the compositions of partial melt from the high-Mg# pyroxenite, and its mineral assemblage is estimated at

250 °C and 10 bar using Theriak-Domino⁶¹ (Extended Data Table 1).

The evolution of mantle potential temperature T_p is solved using the following global heat balance equation⁶²:

$$C \frac{dT_p}{dt} = H - Q, \quad (17)$$

where C is the heat capacity of Earth (7×10^{27} J K⁻¹) and H is internal heat production by ²³⁸U, ²³⁵U, ²³²Th, and ⁴⁰K. Internal heat production is calculated using a parameterization by ref. ⁴³. We assume an initial potential temperature of 1600 °C for both chemically homogeneous and heterogeneous mantles, as explained previously.

The operation of plate tectonics For plate tectonics to operate, the negative buoyancy of the cold lithosphere should be large enough to bend subducting plates. It is noted that the term plate tectonics here refers to a mode of mantle convection that allows for the recycling of the surface layer, and plate kinematics could be different from modern-style plate tectonics. The criterion for plate tectonics is parameterized as⁴⁵

$$\Delta\eta_L \leq 0.25 Ra_i^{1/2} \equiv \Delta\eta_{L,crit}, \quad (18)$$

where $\Delta\eta_{L,crit}$ denotes the critical value for the operation of plate tectonics. For both chemically homogeneous and heterogeneous mantles, the lithospheric viscosity contrast is smaller than the critical value (Extended Data Figure 5), and thus plate tectonics is possible in the Hadean. Because water oceans were likely present at the surface, we consider that thermal cracking weakened the stiff lithosphere⁶³ to reduce the value of effective friction coefficient to $\mu=0.02-0.03$. The existence

of oceans is the key to plate tectonics, because, if water oceans were absent in the Hadean, the value of μ increases to ~ 0.8 , resulting in a large lithospheric viscosity contrast. In such a case, the Hadean Earth would have operated under the stagnant lid mode, which lacks the recycling of the surface.

Mantle degassing by plate tectonics Given that the current rate of plate construction⁵⁸ is $3.4 \text{ km}^2 \text{ yr}^{-1}$ and that the initial depth of mantle melting is $\sim 60 \text{ km}$, the processing rate of the present-day mantle is estimated to be $\sim 6.7 \times 10^{14} \text{ kg yr}^{-1}$, suggesting that it takes $\sim 6 \text{ Gyr}$ to process the entire mantle. For the chemically heterogeneous mantle, plate velocity is faster by ~ 9 times than the present, and the top 2–3 GPa would be dehydrated during the mantle upwelling (see Extended Data Figure 1). Therefore, the processing timescale of the chemically heterogeneous mantle is predicted to be shortened by a factor of 10–15 or to ~ 400 –600 Myr, suggesting that the entire mantle was mostly processed by the end of Hadean. Therefore, the mantle would have become mostly dry by then, and majority of the water budget would reside at the surface.

The fate of iron-rich blobs With a mantle potential temperature of $1600 \text{ }^{\circ}\text{C}$, the high-Mg# pyroxenite matrix would experience $\sim 27\%$ melting, whereas iron-rich blobs would melt up to $\sim 43\%$ when blobs maintain a thermal equilibrium with the pyroxenite matrix (Extended Data Figure 1c). Iron-rich blobs are predominantly consisted of olivine, and the partial melt would be further enriched in iron. The Rhyolite-MELTS model⁴² predicts that such a crust has a composition of MgO 16.0 wt%, FeO 22.9 wt%, SiO₂ 39.2 wt%, Al₂O₃ 9.2 wt%, and CaO 12.6 wt%, resulting in an Mg# of 56 and a crustal density higher than 3500 kg m^{-3} (Extended Data Table 1). The melt

density of partial melt from iron-rich blobs is 3000 kg m^{-3} , which is still lower than the density of the pyroxenite matrix, so the iron-rich melt would migrate upward.

The preexisting lithological heterogeneities (high-Mg# matrix and iron-rich blobs) as well as the newly generated heterogeneities (crustal products and solid residues) would eventually be homogenized as the mantle evolves, but timescale for mixing depends on many uncertain parameters⁶⁴. For example, the subducted iron-rich crust would be denser than ambient mantle, so it may stay longer in the lower mantle without being homogenized with the entire mantle⁵¹. It is not unrealistic to expect that the initial heterogeneity likely survived until the end of the Hadean.

3 Carbon sequestration

The alteration of oceanic crust The alteration of upper oceanic crust is a major source of carbon entering subduction zones^{65,66}, and its flux size was likely to be larger in the Hadean. The upper 500 m of oceanic crust is highly porous, and considering rapid kinetics under high surface temperatures, the porous layer would have efficiently reacted with the seawater. Under an atmospheric pressure over 100 bar, the solubility of CO_2 in water is elevated by more than an order of magnitude⁴⁶, so reactions between silicates within in the upper oceanic and CO_2 would be promoted as well. Ca- and Mg-silicates are thermodynamically susceptible to carbonation under a thick CO_2 atmosphere⁶⁷, so we estimate CO_2 uptake by these silicates within in the upper oceanic crust.

The basis for efficient carbonation is that the Hadean seafloor was supersaturated with respect to carbonate minerals. The modern oceans become undersaturated below 3500–5000 m^{68,69}, but the

carbonate compensation depth was likely to be deeper in the Hadean owing to two main factors⁶⁹: (1) a higher surface temperature due to greenhouse effect and (2) an initially shallower ocean because of the greater water content of the mantle. The amount of water at the surface is estimated to have been less than 10% of the present day in the Hadean (Figure 2), so ocean depth was likely shallower than 500 m. Even with an atmospheric pressure of \sim 200 bar, pressure at the seafloor would be lower than \sim 250 bar. Higher temperatures and lower pressures inhibit the dissolution of carbonates⁶⁹ and thus promote carbonate alteration of the oceanic crust. It is noted that a lower pH due to a thicker CO₂ atmosphere would not be a limiting factor for carbonation. The relative proportion of carbonate ion to the total carbon amount decreases significantly with a lower pH, but carbonate ion concentration would still be larger than the present, or at least remain the same, because the total amount of carbon in the seawater is substantially larger. The actual carbonate ion concentration remains uncertain due to limited experimental data, but the carbonation of oceanic crust is expected to be efficient as long as carbonate ion is present and dissolution is inhibited.

The crust of the chemically heterogeneous mantle would be a mixture of those derived from high-Mg# pyroxenite and Fe-rich blobs, and both components have a large capacity of storing CO₂. Because the formation of carbonates is thermodynamically favorable for Ca- and Mg-silicates under a high CO₂ concentration⁶⁷, we assume that all Ca- and Mg-silicates are used to form carbonates. The crust formed from high-Mg# pyroxenite and Fe-rich blobs both contain \sim 10 wt% of CaO (Extended Data Table 1), so when all Ca-silicates are carbonated, the upper crust would store up to 3.5×10^{19} kg or \sim 7 bar of CO₂. This is 2.7 times of the present-day Earth, where the top 500 m of basaltic crust contains \sim 3.0 wt% of CO₂, equivalent to 1.3×10^{19} kg or \sim 2.5 bar of CO₂⁴⁷. Mg-

silicates, which mostly exist as olivine, orthopyroxene, or clinopyroxene (Extended Data Table 1), are also prone to carbonation⁷⁰, among which olivine has the highest rate of carbonation. The crust of the heterogeneous mantle contains 16–22% of MgO, depending on the relative proportion of high-Mg# and Fe-rich source crusts, so even with a lower bound estimate, the upper crust could contain up to 8.0×10^{19} kg or ~ 15.4 bar of CO₂. This suggests that the seafloor could contain up to ~ 22 bar of CO₂ at one time. Fe-silicates are not considered as a sink for CO₂ because they are more likely to be oxidized to produce H₂.

Carbonates created by hydrothermal alteration would mostly be delivered to the deep mantle under a rapid plate motion. The loss of carbonates in the plate is determined by two factors: (1) the stability of carbonates under a hotter deeper region and (2) the solubility of carbon to water released from the decomposition of hydrous minerals⁶⁶. The stability of carbonates within oceanic crust depends on the *P-T* path of subducting plates, and carbonates are considered to be stable under majority of the modern subduction settings⁶⁵. This is also likely to be the case for the Hadean subduction zones. Although the surface temperature and mantle potential temperature are both hotter by ~ 200 K, the *P-T* path of subducting slab would remain similar to the present-day young subduction zones (Extended Data Figure 3). For the chemically heterogeneous mantle, the rapid plate velocity would allow the slab to be delivered to the deeper region without substantial heating from the surrounding mantle. A pyrolytic homogeneous mantle would have slower plate velocity, but because oceanic plates are older and thus colder, the slab temperature at the deeper region would be similar to that of the heterogeneous mantle. The actual geotherm could vary among different subduction settings even with the same age and plate velocity⁷¹, so the temperature of

some slab surfaces may reach the solidus of carbonate melting⁷². On average, however, the subducting slab is expected to remain colder than the carbonate solidus (Extended Data Figure 3), recycling only a fraction of subducting carbonates back to the surface. Moreover, some fraction of the extracted carbon would be stored in mantle lithosphere and continental crust⁶⁶, the latter of which would have been created by the melting of hydrated subducted materials. Modeling the thermal structure of subduction zones is still subject to large uncertainties as a number of important assumptions are involved, and in this study, we tentatively estimate that 50% of subducted carbonates return to the surface for both pyrolytic and heterogeneous mantles (Figure 4). Whereas the timescale of carbon sequestration would be longer for less efficient carbon subduction, it would always be shorter by an order of magnitude for the case of the heterogeneous mantle.

The loss of carbon may also take place by the dissolution of carbonates to fluid released by serpentine. The Hadean plates, however, are expected to contain \sim 9 times more carbonates than the present-day oceanic crust, and thus it is unlikely for all carbonates to be dissolved. When the top 500 m of oceanic crust contains \sim 10 wt% of water, the maximum amount of CO₂ that could dissolve into serpentinite-driven fluid is 4.4×10^{17} kg, which is less than 1% of total carbonates in oceanic crust. Here, we assume that serpentinization releases water at \sim 3 GPa and the solubility of carbonates to fluid is 10^4 ppm⁶⁶. The amount of water in the underlying crust and mantle is predicted to be limited due to high confining pressure^{73,74}. Considering that the top 30 km includes 0.1 wt% of water, the additional dissolution of CO₂ would be less than 1% of total carbonates in the upper crust. Therefore, the amount of recycled carbon through dissolution is expected to be negligible in the Hadean.

The composition and redox of the atmosphere For both chemically homogeneous and heterogeneous mantles, crust has a higher MgO content and thus forms more olivine. The dissolution of olivine is efficient compared to other silicate minerals, and thus following reactions are likely to occur:



where each reaction represents oxidation of ferrous iron and serpentinization of forsterite. We assume that all fayalite would be oxidized to form magnetite by Reaction (19). The serpentinization of forsterite would consume SiO_2 and thus promotes the oxidation of iron and the carbonation of other minerals.

The amount of hydrogen production differs between the chemically homogeneous and heterogeneous mantles because of their difference in mineral assemblage of the seafloor. Crust with a lower Mg# contains more iron and thus produces more H_2 . Following the stoichiometry of reactions, 0.07 mol of H_2 is estimated to be released to the atmosphere per 1 mol of olivine in the case of the homogeneous pyrolytic mantle, whereas 0.04 mol of H_2 is released for the chemically heterogeneous mantle. The H_2 production rate, however, is higher for the chemically heterogeneous mantle because the seafloor is renewed at a rate ~ 10 times faster than the homogeneous pyrolytic mantle (Figure 4a).

The composition of the atmosphere is calculated using Gibbs free energy minimization, the implementation of which is described in ref. ⁷⁵. We calculate equilibrium under temperature and

pressure conditions at the bottom of the atmosphere. CO_2 , CO , CH_4 , H_2O , and H_2 are considered are possible species. In reality, the atmospheric composition is affected by photochemical reactions. Such an effect, however, is not included because our aim is to provide a zeroth-order estimate on the change in redox state with active carbonation and serpentinization.

Subduction geotherms The P - T path of Extended Data Figure 3 is calculated using the model of ref. ⁷⁶. The age of subducting plate is assumed to be 10 Myr with a slab dip angle of 45° , but the angle does not have a significant influence on the geotherm. For an activation energy for viscosity, the value of 300 kJ mol^{-1} is adopted. Because the model assumes an incompressible fluid, the modeled potential temperature is converted to the actual value using an adiabatic gradient of 0.5 K km^{-1} .

Atmospheric model The surface temperature of the atmosphere is calculated using a 1-D radiative-convective atmosphere model of ref. ⁵². This model assumes that the atmosphere is gray to outgoing infrared radiation but transparent to incoming solar visible radiation. The atmosphere consists of two layers, stratosphere and troposphere. The former is in radiative equilibrium, whereas the latter is saturated with water, and its thermal profile is governed by wet adiabatic gradient (see Supplementary for details). We assume that the early Earth atmosphere contains 1 bar of N_2 with a varying mixture of CO_2 and H_2O , which are determined based on the partitioning of volatiles between a magma ocean and the atmosphere. Sulfur and chloride volatiles may have also contributed to the greenhouse effect⁷⁷, but its effect is likely to be smaller compared to that created by a thick atmosphere of CO_2 and H_2O .

We use a solar constant 30% smaller than the present to account for the faint young Sun, and the planetary albedo is fixed at 0.3. The hydrodynamic escape of volatiles is not included in this model for simplicity, although its effect would be significant for the case of homogeneous mantle, whose evolutionary timescale exceeds 1 Gyr.

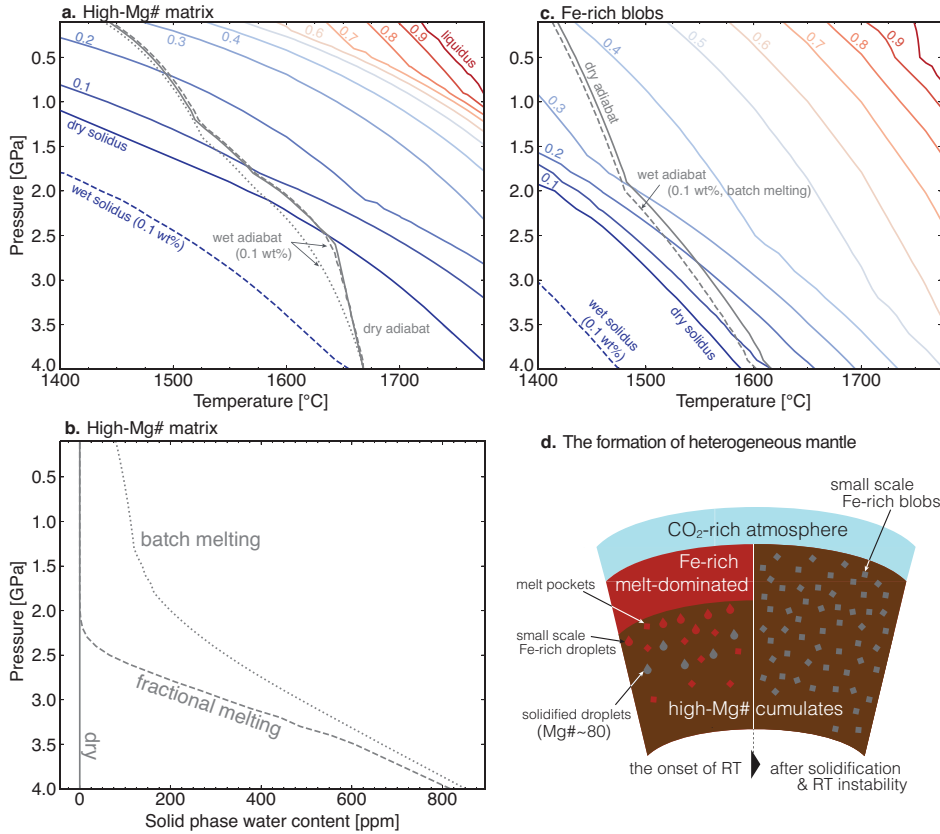
Data Availability All relevant data are provided in the paper. Codes to reproduce the results are available at <https://github.com/yoshi-miyazaki/Hadean-evolution/>. Gibbs energy minimization code is available at <https://github.com/yoshi-miyazaki/GibbsE-minimization/>.

Acknowledgements This work was sponsored by the U.S. National Aeronautics and Space Administration under Cooperative Agreement No. 80NSSC19M0069 issued through the Science Mission Directorate and the National Science Foundation under grant EAR-1753916. This work was also supported in part by the facilities and staff of the Yale University Faculty of Arts and Sciences High Performance Computing Center. Y.M. was supported by the Stanback Postdoctoral Fellowship from Caltech Center for Comparative Planetary Evolution. The authors thank Norman Sleep and Marc Hirschmann for providing constructive comments, which were helpful to substantially improve the accuracy of the manuscript.

Author Contributions Y.M. and J.K. designed the study, discussed the results, and wrote the manuscript. Y.M. performed calculations.

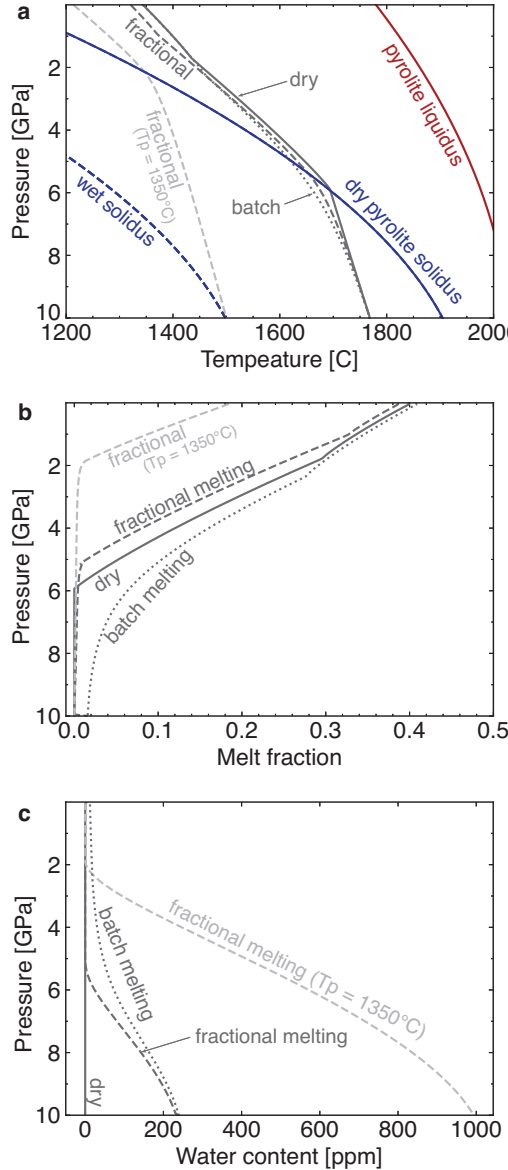
Competing Interests The authors declare no competing financial interests.

Correspondence Correspondence and requests for materials should be addressed to Y.M. (email: ymiya@caltech.edu).

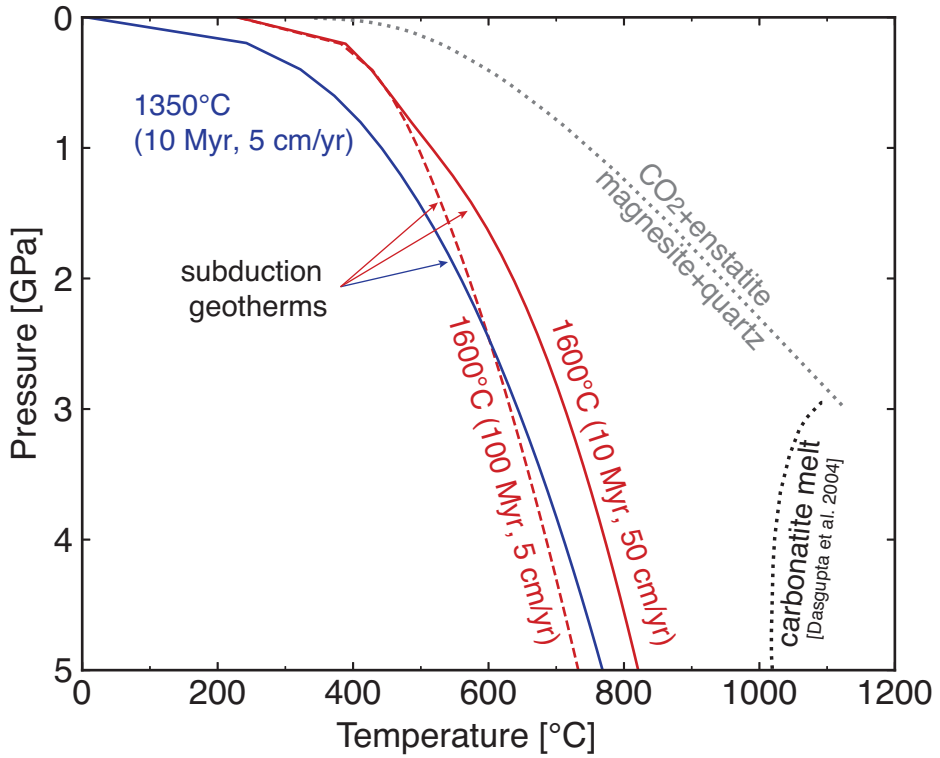


Extended Data Figure 1: The thermal structure of the chemically heterogeneous mantle plotted together with contours of melt fraction.

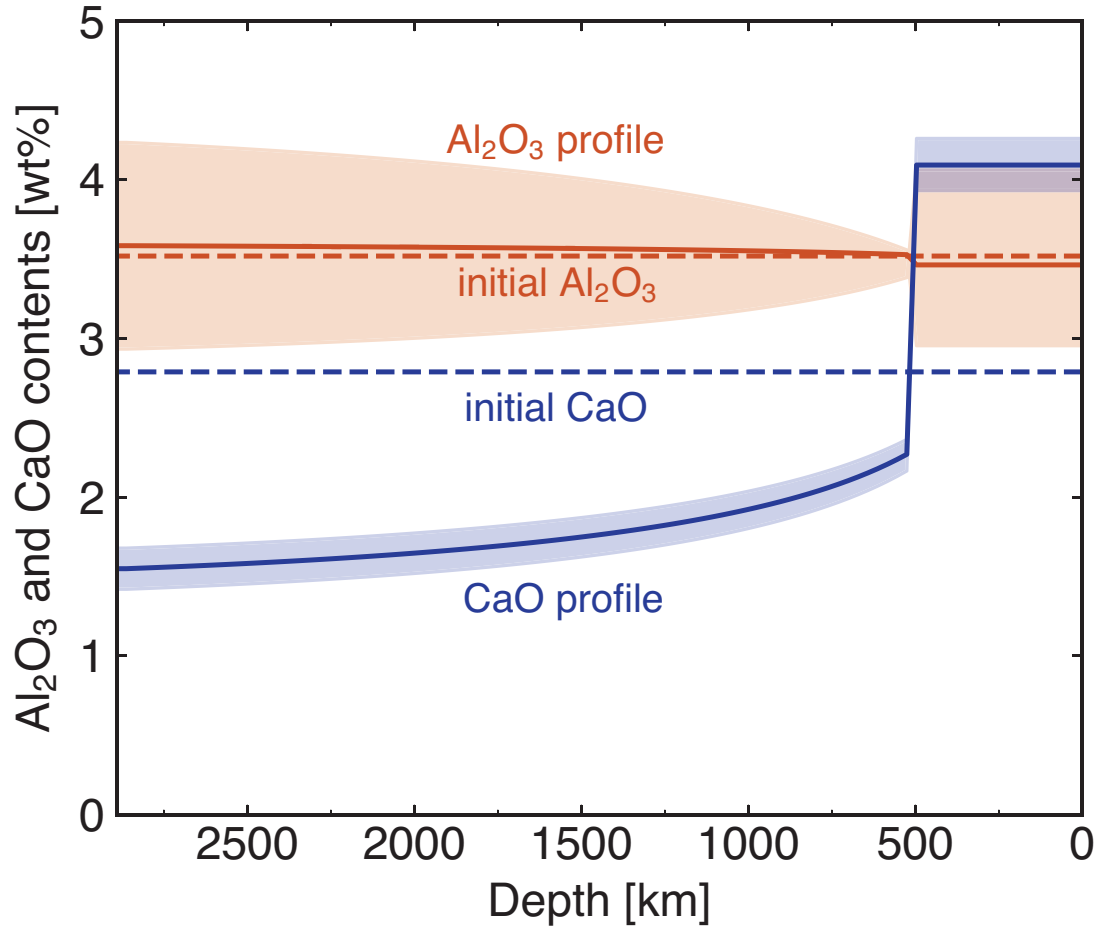
a–c. Melt fraction is shown for two components of the mantle, **a.** high-Mg# pyroxenite matrix and **c.** Fe-rich blobs, and **b.** water content remaining in the solid phase of the high-Mg# matrix. The melt fractions of high-Mg# matrix and Fe-rich blobs are estimated using the Rhyolite-MELTS model⁴². The dry (gray solid) and wet (0.1 wt%; gray dashed) adiabats are calculated with a potential temperature of 1600 °C, using Equation (S1) in Supplementary. For the wet adiabat of the high-Mg# matrix, two modes of melting are considered, batch (dotted) and fractional (dashed), and for the latter, we assume that 90% of melt would escape from the mantle for every 0.1 GPa of ascent when the degree of melting is greater than 1%. The fraction of melt escaping the system is insensitive to the thickness of complete dehydration, and values between 10% and 99.9% would yield a thickness within 0.1 GPa of what is predicted in this figure. **d.** Schematic illustration of the compositional structure of the mantle during and after the solidification of a magma ocean under fractional crystallization. The mantle experiences global-scale chemical stratification, leaving an Fe-rich layer near the surface. Such stratification is subject to the Rayleigh-Taylor (RT) instability, resulting in the dripping-like descent of Fe-rich materials. This period corresponds to Figure 1a. These droplets would solidify as they sink through the mantle (left) and be mixed with high-Mg# cumulates. When the surface becomes rheologically solid (Figure 1b), the mantle would have a structure with small-scale chemical heterogeneity, embedded in high-Mg# matrix (right).



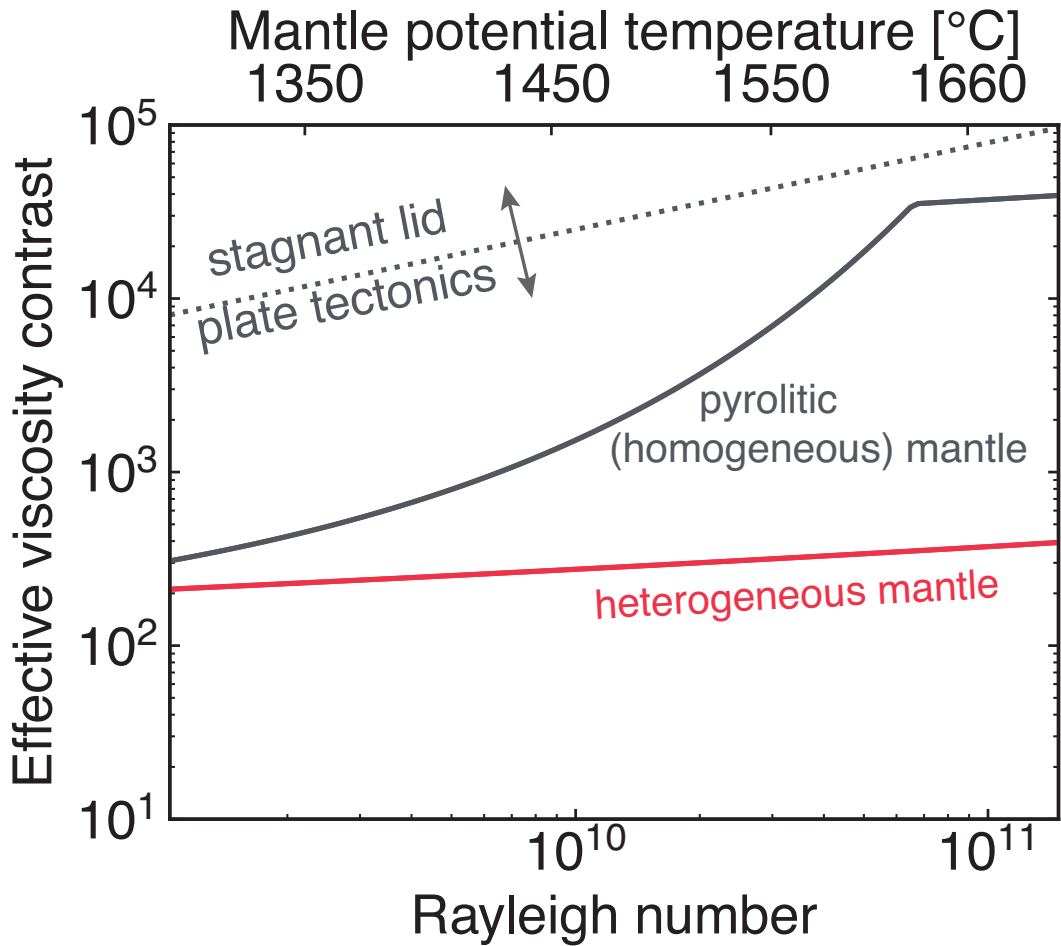
Extended Data Figure 2: Thermal structure of a pyrolytic (chemically homogeneous) mantle when a melt-dominated layer disappears. The figure describes when the entire mantle starts to behave rheologically as solid, which corresponds to a potential temperature of ~ 1600 °C. The profiles of **a.** temperature, **b.** melt fraction, and **c.** water content are shown for both dry (gray solid) and wet (0.1 wt%; gray dotted and dashed) mantles, together with the solidus (blue) and liquidus of pyrolite (red). The solidus of a wet mantle (blue dashed) is estimated using Equation (S2) in Supplementary and a melt/mineral partitioning coefficient of $D=0.005$. Two modes of melting are considered for the wet mantle, batch (dotted) and fractional (dashed). Temperature profiles would be adiabatic as a result of the Rayleigh-Taylor instability, and melt fraction is estimated using a model of ref. ²⁴ with the mass fraction of clinopyroxene of 19 wt%. For fractional melting, we assume that 90% of melt would escape from the mantle for every 0.1 GPa of ascent when the degree of melting is greater than 1%.



Extended Data Figure 3: **The subduction geotherm during the Hadean with the stability field of carbonates.** P - T paths are calculated assuming a dip angle of 45° using the model of ref. ⁷⁶ (see Methods for details). We consider (1) a mantle potential temperature of 1350 $^\circ\text{C}$ with a plate age of 10 Myr, a velocity of 5 cm yr^{-1} , and a surface temperature of 0 $^\circ\text{C}$ (blue), (2) a potential temperature of 1600 $^\circ\text{C}$ with a plate age of 10 Myr, a velocity of 50 cm yr^{-1} , and a surface temperature of 230 $^\circ\text{C}$ (red solid), and (3) a potential temperature of 1600 $^\circ\text{C}$ with a plate age of 100 Myr, a velocity of 5 cm yr^{-1} , and a surface temperature of 230 $^\circ\text{C}$ (red dashed), representing the present-day young slab, the Hadean slab of the chemically heterogeneous mantle, and that of a homogeneous pyrolytic mantle, respectively. P - T paths of the heterogeneous and homogenous mantles are similar because rapid plate motion mitigates the heating of the slab from the surrounding mantle. The solidus of carbonate melt is adopted from ref. ⁷² (black dotted), and the decomposition of magnesite under the presence of quartz is calculated using Theriak-Domino⁶¹ (gray dotted).



Extended Data Figure 4: **The profiles of Al_2O_3 (red) and CaO (blue) contents after magma ocean solidification.** Profiles before the onset of small-scale Rayleigh-Taylor instabilities are shown. The top 500 km of the mantle becomes the source for iron-rich blobs, whereas the lower mantle composition corresponds to the high-Mg# matrix in the main text. We assume that newly formed crystals in the magma ocean would stack at the base of the melt-dominated layer (Figure 1a). Initial concentrations of Al_2O_3 3.5 wt% and CaO 2.8 wt%⁷⁸ are assumed (dashed lines), and partitioning coefficients between melt and bridgemanite are calculated from the experimental results of Tronnes and Frost⁵⁶ and Corgne et al.⁵⁷ Shaded areas represent uncertainties, which are calculated using partitioning coefficients 30% larger and smaller values than the mean estimated values ($D_{\text{Al/Si}} = 0.78$ and $D_{\text{Ca/Si}} = 0.16$).



Extended Data Figure 5: **Effective viscosity contrast across the lithosphere and the criteria for plate tectonics.** Effective viscosity contrast is shown (Equation (14)) as a function of the internal Rayleigh number, together with the corresponding mantle potential temperature. The thickness of depleted lithospheric mantle h_m in Equation (14) is different between chemically homogeneous (gray) and heterogeneous mantles (red), and the values of h_m are shown in Figure 3b. The criteria for plate tectonics ($\Delta\eta_{L,crit}$ in Equation (18)) is also plotted with a dotted line.

	SiO ₂	MgO	FeO	Al ₂ O ₃	CaO	olivine	opx	cpx	feldspar	others	density
	[wt%]					[wt%]					[kg/m ³]
High-Mg# crust ^a	43.6	21.5	5.3	18.9	10.7	20.9	21.5	26.9	18.5	12.1 ^d	3010 ^g
High-Mg# DLM	52.0	41.5	4.2	1.8	0.5	33.4	64.7	1.9	-	-	3120
High-Mg# pyroxenite	51.3	39.5	4.1	3.5	1.5	24.9	69.8	-	-	5.2 ^d	3130
Iron-rich crust ^b	39.2	16.0	22.9	9.2	12.6	38.9	-	46.3	1.5	13.4 ^e	3570 ^h
Iron-rich DLM	33.9	45.5	18.1	1.61	1.02	85.2	-	-	-	14.8 ^e	3340
Iron-rich blobs	35.3	37.8	19.0	3.7	4.1	84.0	-	-	-	16.0 ^e	3350
Modern MORB ^c	50.47	7.58	10.43	14.7	9.4	9.3	11.6	24.1	51.4	3.5 ^f	3030

Extended Data Table 1: Compositions of high-Mg# pyroxenite, iron-rich blobs, and their differentiated components. Mineral proportions and densities are calculated using Theriaak-Domino⁶¹ under 250 °C and 10 bar for crustal components and 1500 °C and 1.2 GPa for mantle components. DLM indicates depleted lithospheric mantle, which is calculated as the depleted residue of partial melting.

- a. From the partial melt of pyroxenite at 1570 °C and 1.8 GPa with 11 % melting.
- b. From the partial melt of iron-rich blob at 1520 °C and 2.3 GPa with 28 wt% melting.
- c. From ref. ⁷⁹. The total of oxides is lower than 100 % because other minor oxides, including Na₂O and TiO₂, are not shown here.
- d. The high-Mg# pyroxenite contains spinel, whereas crust contains corundum.
- e. Iron-rich blobs and its depleted reservoir include merwinite, spinel, and periclase, whereas iron-rich crust only contains spinel.
- f. Mid-ocean ridge basalt contains ilmenite as a Ti-bearing phase.
- g. Before crystallization, the melt density of partial melt from the high-Mg# pyroxenite is 2660 kg m⁻³.

The melt density is calculated using the Rhyolite-MELTS model⁴² at a temperature of 1500 °C and 10 bar. Under a mantle condition of 1500 °C and 1.2 GPa, the density increases to 3180 kg m⁻³, and it is likely to be heavier than the ambient mantle.

- h. Before crystallization, the melt density of partial melt from iron-rich blobs is 3000 kg m⁻³. The melt would thus migrate upwards within the pyroxenite matrix. Its density under the mantle condition is estimated to be 3440 kg m⁻³.